Coastal Engineering 210 (2026) 105052

Contents lists available at ScienceDirect

Coastal Engineering

journal homepage: www.elsevier.com/locate/coastaleng

Nonlinear evolution of wave groups over a rectangular step: Characteristics of superharmonics

Qian Wu [a,b], Xingya Feng [b,*], You Dong [c], Wooyoung Choi [d], Frédéric Dias [e,f]

[a] Marine Hydrodynamic Research Facility, The Hong Kong University of Science and Technology (Guangzhou), Nansha, Guangzhou 511400, China
[b] Department of Ocean Science and Engineering, Southern University of Science and Technology, Shenzhen 518055, China
[c] Department of Civil and Environmental Engineering, The Hong Kong Polytechnic University, 999077, Hong Kong, China
[d] Department of Mathematical Sciences, New Jersey Institute of Technology, Newark, NJ 07102-1982, USA
[e] School of Mathematics and Statistics, University College Dublin, Dublin, Ireland
[f] Centre Borelli, École Normale Supérieure Paris-Saclay, Gif-sur-Yvette, 91190, France

ARTICLE INFO

Keywords:
Harmonic analysis
Topographic effect
Free and bound waves
Focused wave groups

ABSTRACT

Focused wave groups are often used to study extreme waves in the laboratory, yet their nonlinear evolution over abrupt bathymetric features remains inadequately understood. This is particularly true for rectangular steps, a configuration relevant to both natural seabed forms and coastal structures. This paper combines physical experiments with a fully nonlinear potential flow model to investigate the transformation of such wave groups over a submerged rectangular step. By integrating a phase-manipulation technique with a continuous wavelet transform, we achieve unprecedented spatio-temporal separation and tracking of superharmonic components. This approach yields the first clear experimental and numerical evidence of the coexistence and distinct evolution of second-order bound and free waves over the step. Two key nonlinear mechanisms induced by the step are identified and quantified: (i) superharmonic interactions that enhance wave crest amplitudes by up to 79% compared to flat-bottom conditions, and (ii) harmonic phase modulation that systematically shifts the wave focusing position downstream by 0.1–0.4 peak wavelengths. These findings provide new physical insight into extreme wave amplification over complex bathymetry, with direct implications for coastal hazard assessment and the design of marine infrastructure.

1. Introduction

The interaction of water waves with abrupt changes in seabed topography, such as submarine trenches, continental shelf edges, and engineered structures like stepped revetments, is a fundamental problem in coastal and ocean engineering. The canonical case of the rectangular step, despite its geometrical simplicity, captures the essential physics of wave reflection, transmission and most critically, nonlinear energy transfer among a broad spectrum of harmonics (Mondal and Alam, 2018; Massel, 1983). Understanding these processes is significant for predicting and mitigating the impact of extreme waves on offshore structures and coastal infrastructures (Liu et al., 2026; Li et al., 2023).

Early research on wave–seabed interaction effectively addressed linear and weakly nonlinear regimes. Seminal work, such as the study of Kirby and Dalrymple (1983) on wave propagation over trenches, offered insight into the scattering properties of submerged obstacles. Subsequently, the systematic laboratory experiments of Beji and Battjes (1993) on wave propagation over a bar documented the generation of free higher harmonics induced by the varying bathymetry. Extensive analytical and numerical studies have addressed such transformations over bottom steps (Kurkin et al., 2015; Ducrozet et al., 2021; Negi et al., 2025). These works helped clarify that the linear superposition fails to capture the strong nonlinear interactions triggered by abrupt depth changes. This foundational understanding paved the way for investigating extreme wave generation, with numerous studies confirming that an abrupt depth transition can significantly enhance the kurtosis of the surface elevation. This leads to a heavier-tailed distribution of wave heights, thereby increasing the probability of extreme wave occurrence (Samseth and Trulsen, 2025; Li and Chabchoub, 2023; Moore et al., 2020; Trulsen et al., 2020; Gramstad et al., 2013). For instance, Zhang et al. (2023) demonstrated that for random waves, the Rayleigh distribution systematically underestimated the exceedance probability of wave heights in the lee of an infinite step, a statistical anomaly corroborated by both laboratory experiments (Trulsen et al., 2012) and numerical simulations (Viotti and Dias, 2014).

The physical mechanisms underpinning these statistical observations are primarily rooted in nonlinear wave–wave interactions and

* Corresponding author.
E-mail address: fengxy@sustech.edu.cn (X. Feng).

https://doi.org/10.1016/j.coastaleng.2026.105052
Received 18 December 2025; Received in revised form 6 May 2026; Accepted 8 May 2026
Available online 13 May 2026
0378-3839/

energy transfer to superharmonics (Draycott et al., 2022; Benoit et al., 2024). For simple waveforms like monochromatic waves, this process is relatively well understood. However, monochromatic waves cannot represent the complex interactions inherent in realistic sea states. For instance, analytical studies by Li et al. (2021a) on focused wave groups revealed distinct forcing mechanisms for second-order free waves over depth transitions, while Moss et al. (2025) demonstrated the critical impact of these superharmonics on wave loads. These findings underscore the necessity of investigating nonlinear waves to accurately capture hydrodynamic behaviors in complex bathymetries.

In light of this, recent studies have increasingly investigated directional and focused wave groups to represent extreme waves better. The propagation of these wave groups over variable bathymetry introduces additional complexities, including directional effects (Tang et al., 2023) and the interplay between nonlinearity and two-dimensional bathymetric features (Draycott and Li, 2025). The analysis of such complex wave fields necessitates advanced techniques capable of resolving the spatio-temporal evolution of individual harmonic components. For instance, Li et al. (2021a) relied on sufficient propagation distance to spatially separate bound and free harmonics due to their distinct phase speeds. Numerically capturing these processes poses significant challenges. While Computational Fluid Dynamics (CFD) methods can resolve these details, they are often computationally inpractical for extensive parameteric studies. Conversely, weakly nonlinear potential flow models may fail to capture the strong nonlinearities during wave–structure interaction. Therefore, the fully nonlinear potential flow (FNPF) theory emerges as an optimal balance, offering high computational efficiency while satisfying nonlinear free-surface boundary conditions exactly (Liu et al., 2026; Zheng et al., 2020; Viotti and Dias, 2014). In this study, we employ an efficient FNPF model based on the conformal mapping method (Choi and Camassa, 1999; Viotti et al., 2014), which effectively eliminates the singularities at sharp topographic features like a step corner.

Despite these advances, a pivotal and unresolved challenge is the detailed spatio-temporal separation and tracking of superharmonics during the propagation of focused wave groups over a rectangular step. While existing literature has extensively studied overall wave transformation and statistical properties (Bolles et al., 2019; Li et al., 2021b; Zhang and Benoit, 2021), detailed experimental evidence regarding the distinct spatio-temporal evolution of second-order bound and free waves remains limited. These components, despite coexisting at the same frequency range, propagate at different phase speeds and exhibit fundamentally different physical characteristics (Schäffer, 1996). The second-order bound waves are locked to the primary wave group, while the free waves, once generated, propagate at their own intrinsic speed and can travel behind the group, potentially influencing the wave field far from the point of generation. Although the recent experimental and numerical work of Moss et al. (2025) has begun to quantify the contributions of these harmonics, a comprehensive and clear tracking of their distinct spatial evolution is still lacking.

The primary novelty of this study, therefore, lies in the integrated application of a phase-manipulation technique and continuous wavelet transform (CWT) to experimentally and numerically separate and track the evolution of the first four harmonics. This methodology enables the unique identification and spatio-temporal tracking of second-order bound and free waves. It is supported by numerical simulations based on the FNPF model and the conformal mapping method. By analyzing the amplitude, spectral width and waveform profiles of focused wave groups, this research reveals the influence of a rectangular step on nonlinear wave propagation, providing mechanistic insights that are crucial for improving the prediction of extreme wave events in coastal regions with complex bathymetry.

The aim of this study is to elucidate the superharmonic evolution, particularly the genesis and role of second-order free waves, in focused wave groups propagating over a rectangular step. The organization of this paper is as follows. Section 2 describes the laboratory experiments and the FNPF numerical model based on the conformal mapping method. Section 3.1 presents the spatial variation of wave crests and the evolution of wave spectra. A detailed harmonic analysis is performed in Section 3.2, comparing results over a constant depth and the rectangular step, and demonstrating the crests of the separated second-order bound and free waves. Then, the analysis of skewness and kurtosis is presented in Section 3.3. Finally, the conclusions are summarized in Section 4.

2. Methods

2.1. Experimental setup

A series of experiments were conducted in the Hydrodynamic Laboratory at the Southern University of Science and Technology. The experiments were carried out in a wave flume with the following dimensions: 20 m long, 1.2 m deep, and 0.8 m wide, as displayed in Fig. 1. The flume was equipped with a piston-type wavemaker and a porous absorber at the end to minimize the influence of reflected waves. A stainless steel step was placed in the middle section of the flume, with its upstream side positioned 7.5 m away from the wavemaker. The rectangular step was 2.4 m long and 0.24 m high. To make observations easier, we placed the origin of the coordinate system on the free surface of the middle section of the step, 8.7 m from the wavemaker, and in the direction of wave propagation. Two depths of water are considered: $h_d = 0.36$ m and $h_d = 0.48$ m. These achieve depth ratios of 1/3 and 1/2 between the shallower and deeper regions, respectively. The positions of the 20 capacitive-type wave gauges were carefully chosen, with half of them being placed at depth changes and the other half being placed near both ends of the flume. These positions are listed in Table 1, with WG 10 located at the midpoint of the step.

This study investigates the propagation of focused wave groups under both constant depth and rectangular step conditions. The focusing position is located at $x_f = -1.0$ m (corresponding to WG 6, located 7.7 m from the wavemaker), with a focusing time of $t_f = 30$ s. Because wave nonlinearity naturally shifts the focal position (Monsalve et al., 2022), uncalibrated waves would encounter the step at different evolutionary stages. Consequently, wavemaker inputs were iteratively adjusted to ensure actual focusing occurred precisely at WG 6 for all constant-depth cases. Establishing this uniform physical baseline guarantees that any subsequent focal shifts observed in the step cases are solely attributable to the bathymetric transition. Specifically, the fluid domain is characterized by an initial deeper water depth h_d, which abruptly transitions to a shallower water depth h_s over the rectangular step. The incident focused wave groups are primarily defined by their target linear amplitude a, peak frequency f_p, and the corresponding peak wavenumber k_p. The detailed combinations of these parameters for all test cases are summarized in Table 2. Both k_p and k_{ps} are derived from f_p based on the linear dispersion relation corresponding to their local water depths (h_d and h_s, respectively).

2.2. Computational model

A two-dimensional fully nonlinear numerical model in the (x, y) plane is established using the conformal mapping method. In the mathematical model, the fluid is incompressible and inviscid, with irrotational flow. Within the potential flow theory framework, the velocity potential $\phi(x, y, t)$ is governed by the Laplace equation. The free surface displacement, described by $y = \eta(x, t)$, satisfies both the kinematic and dynamic boundary conditions, while the seabed is considered impermeable. The governing equations and boundary conditions are expressed as follows:

$$\frac{\partial^2 \phi}{\partial x^2} + \frac{\partial \phi}{\partial y^2} = 0 \quad \text{for} \quad -h(x) \leq y \leq \eta(x, t), \tag{1}$$

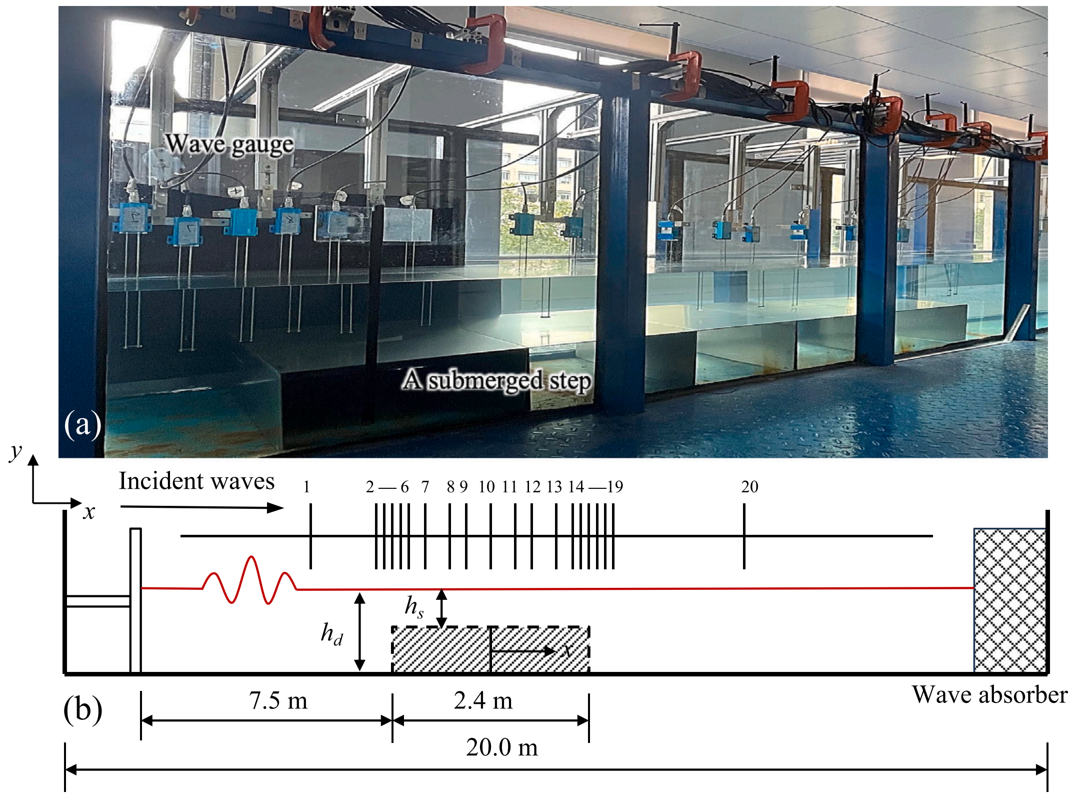

Fig. 1. (a) A two-dimensional wave flume with a rectangular step and (b) a sketch of the experimental wave flume with 20 wave gauges.

Table 1
Positions of the twenty wave gauges are shown in Fig. 1.

WG No.	WG 1	WG 2	WG 3	WG 4	WG 5	WG 6	WG 7	WG 8	WG 9	WG 10
Position (m)	−2.2	−1.4	−1.3	−1.2	−1.1	−1.0	−0.8	−0.5	−0.3	0
WG No.	WG 11	WG 12	WG 13	WG 14	WG 15	WG 16	WG 17	WG 18	WG 19	WG 20
Position (m)	0.3	0.5	0.8	1.0	1.1	1.2	1.3	1.4	1.5	3.0

Table 2
Selected case parameters with a rectangular step. The Ursell number is defined as $U_r = \frac{H_d}{h_s}(\frac{\lambda}{h_s})^2$, where H_d represents twice the wave amplitude $2a$ before the step. All cases are repeated at least three times.

Case	h_d (m)	h_s/h_d	f_p (Hz)	k_pa	k_ph_d	$k_{p_s}h_s$	U_r	Case	h_d (m)	h_s/h_d	f_p (Hz)	k_pa	k_ph_d	$k_{p_s}h_s$	U_r
1	0.36	1/3	0.8	0.08	1.139	0.586	115.42	10	0.48	1/2	0.8	0.08	1.397	0.877	18.52
2	0.36	1/3	0.9	0.06	1.345	0.669	52.62	11	0.48	1/2	0.9	0.06	1.678	1.018	8.02
3	0.36	1/3	0.9	0.08	–	–	70.16	12	0.48	1/2	0.9	0.08	–	–	10.70
4	0.36	1/3	0.9	0.10	–	–	87.70	13	0.48	1/2	1.0	0.08	2.003	1.171	6.29
5	0.36	1/3	0.9	0.12	–	–	105.24	14	0.48	1/2	1.1	0.08	2.378	1.340	3.76
6	0.36	1/3	0.9	0.14	–	–	122.78								
7	0.36	1/3	1.0	0.08	1.578	0.756	43.43								
8	0.36	1/3	1.1	0.08	1.843	0.847	27.24								
9	0.36	1/3	1.2	0.08	2.144	0.944	17.30								

$$\frac{\partial \eta}{\partial t} + \frac{\partial \phi}{\partial x}\frac{\partial \eta}{\partial x} - \frac{\partial \phi}{\partial y} = 0 \quad \text{at} \quad y = \eta(x,t), \tag{2}$$

$$\frac{\partial \phi}{\partial t} + \frac{1}{2}\left(\frac{\partial^2 \phi}{\partial x^2} + \frac{\partial^2 \phi}{\partial y^2}\right) + g\eta = 0 \quad \text{at} \quad y = \eta(x,t), \tag{3}$$

$$\frac{\partial \phi}{\partial n} = 0 \quad \text{at} \quad y = -h(x), \tag{4}$$

where n denotes the normal vector on the boundaries, g represents the acceleration due to gravity, and $h(x)$ denotes the water depth. Specifically, for the rectangular step topography, Eq. (4) enforces $\frac{\partial \phi}{\partial y} = 0$ at the horizontal bottom ($y = -h_d$ and $y = -h_s$) and $\frac{\partial \phi}{\partial x} = 0$ at the vertical sides of the step. A periodic boundary condition is applied in the direction of wave propagation. To reduce the influence of reflected waves from the end of the numerical domain, an additional pressure term P_S is incorporated into the dynamic free-surface boundary condition to act as an absorbing layer (Fig. 2). The spatial weight function $s(x)$ governs the smooth transition of the damping intensity and is defined as $s(x) = e^{(-[(x-L_w)/2]^2)}$, where L_w denotes half the length of the numerical wave tank. Accordingly, Eq. (3) is modified as

$$\frac{\partial \phi}{\partial t} + \frac{1}{2}\left(\frac{\partial^2 \phi}{\partial x^2} + \frac{\partial^2 \phi}{\partial y^2}\right) + g\eta + \frac{P_S}{\rho} = 0, \tag{5}$$

$$\frac{P_S}{\rho} = s(x)\phi(x, \eta(x,t), t). \tag{6}$$

To efficiently solve the boundary value problem, a time-dependent conformal mapping technique is employed. This approach maps the physical fluid domain, bounded by a time-varying free surface, onto

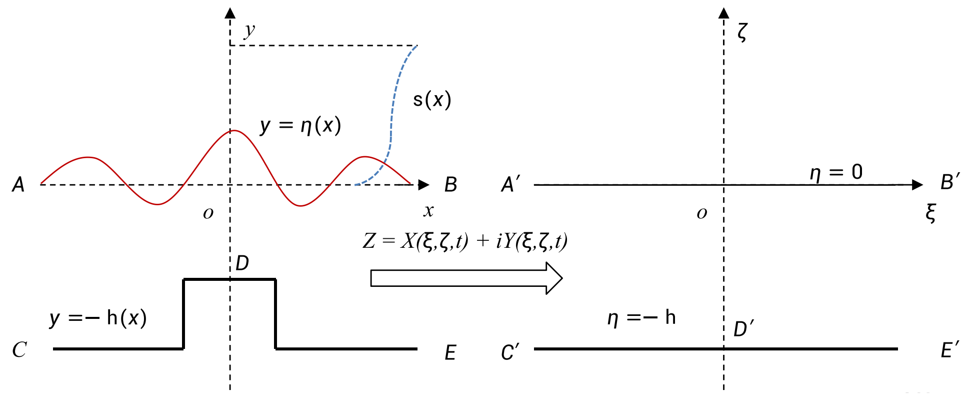

Fig. 2. Schematic diagram of the transformation in the conformal mapping method.

a uniform strip in the mathematical plane. Governed by the Cauchy-Riemann relations, the complex velocity potential and spatial coordinates are analytically coupled within the conformal domain. By applying the Cauchy integral operator, the surface kinematics are explicitly resolved without solving the Laplace equation throughout the entire fluid interior. Consequently, this transformation significantly simplifies the free-surface boundary conditions, eliminating the need to solve Laplace's equation on varying boundaries. The reformulated equations are discretized via a pseudo-spectral method and subsequently solved using an iterative time-marching scheme. The iteration continues until the residual falls below a threshold of 1×10^{-10}, after which the process advances to the next iteration. For time integration, an adaptive Adams–Bashforth–Moulton method is implemented. This multi-step scheme enforces a strict error tolerance, utilizing data from the previous 13 time steps to estimate errors, making it well-suited for simulating dynamic wave evolution. A comprehensive mathematical derivation of the mapping functions and associated operators is detailed in Wu et al. (2023). The fully nonlinear numerical model is able to capture the detailed wave evolution in the temporal and spatial domains. To avoid wave breaking, the steepness of peak wave components is maintained at $k_p a \leq 0.14$, a condition that maintains high numerical accuracy (Viotti and Dias, 2014). Furthermore, the convergence of numerical results was extensively examined by varying the number of discrete points, as detailed in Appendix A.

The present numerical approach employs a mapping technique to efficiently simulate nonlinear wave propagation, including cases involving complex bathymetry such as a rectangular step. It should be noted that to reconcile the fundamental discrepancy between physical models (boundary-value problems) and numerical models (initial-value problems), both methods allow waves to evolve naturally over a sufficient distance, thereby producing a consistent wave field at the focal point. The physical model's linear theory generates spurious free waves, causing slight temporal discrepancies in the propagation of second-order free waves between the physical and numerical results (e.g., Fig. 15 in Section 3.2.3). However, this initial limitation does not critically alter the primary nonlinear transformation processes over the step. Overall, the mapping-based numerical method proves effective in simulating nonlinear wave propagation (Viotti et al., 2014; Choi and Camassa, 1999), even over bathymetry with abrupt depth changes.

2.3. Focused wave group

The initial wave surface elevation $y(\xi)$ is prescribed by the mathematical form of the desired incident wave type. The adaptive algorithm then initiates an iterative process to advance the solution in time. Through this process, fully nonlinear results in the target regimes are obtained within the framework of the Euler equations. Owing to this setup, the incident wave type can be readily modified at the initial step. It should be noted that this numerical generation approach differs slightly from the wavemaker used in laboratory experiments because it uses a spatial linear wave pattern at time $t = 0$ as the initial condition. The analysis concentrates on the steady solution in the vicinity of the step, where nonlinear dynamics have fully developed. Potential influences from initial transients, such as spurious free waves, are minimized since the region of interest is situated sufficiently far from the numerical boundaries.

Focused wave groups have been widely used in laboratory research to study extreme wave conditions (Salis et al., 2024). By adjusting the initial phase of each wave component, these wave groups can be designed to reach their maximum amplitude at a predefined location. The linear theory for focused wave groups, initially formulated by Rapp and Melville (1990), is based on the superposition of multiple wave components with amplitudes A_i. When the wavenumber k_i, angular velocity ω_i and phase velocity c_i satisfy the linear dispersion relation, the surface elevation and velocity potential of a focused wave group are as follows:

$$\eta(x,t) = \sum_{i=1}^{n} A_i \cos[k_i((x - x_f) - c_i(t - t_f)) + \phi_0], \tag{7}$$

$$\phi(x,t) = \sum_{i=1}^{n} A_i c_i \frac{\cosh(k_i h_d)}{\sinh(k_i h_d)} \sin[k_i((x - x_f) - c_i(t - t_f)) + \phi_0], \tag{8}$$

where the focusing position x_f and focusing time t_f are selected to generate the maximum wave amplitudes at the prescribed condition. Incoming waves are considered with initial phase shifts ϕ_0 of 0°, 90°, 180° and 270°. The number of wave components in a focused wave group is set to $n = 2000$.

The frequency bandwidth $f/f_p \in [0.3, 1.8]$ encompasses a range of frequencies. The amplitude A_i of each component is given by a JONSWAP-type spectrum

$$S(f_i) = \beta H_s^2 T_p^{-4} f_i^{-5} exp[-\frac{5}{4}(T_p f_i)^{-4}]\gamma^{\exp[-(f_i/f_p-1)^2/2\sigma^2]}, \tag{9}$$

$$\beta = \frac{0.06238}{(0.23 + 0.0336\gamma) - 0.185(1.9 + \gamma)^{-1}}[1.094 - 0.01915\ln(\gamma)], \tag{10}$$

$$A_i(f_i) = A\frac{S(f_i)\Delta f}{\sum_{i=1}^{n} S(f_i)\Delta f}, \tag{11}$$

where the frequency interval is given by $\Delta f = (1.8 - 0.3)f_p/(2000 - 1)$, and the peak wave period is $T_p = 1/f_p$. The peak enhancement parameter γ is 3.30. The spectral width parameter σ is set to 0.07 for $\omega_i \leq \omega_p$ and 0.09 for $\omega_i > \omega_p$. Due to the nonlinear wave–wave interactions, the linear amplitude of the focused wave group $A = \sum_{i=1}^{n} A_i$ is greater than the maximum focal crest amplitude a over a flat seabed. To investigate the effect of the rectangular step, the amplitude a is used to define all amplitude-related parameters, including the wave steepness ka.

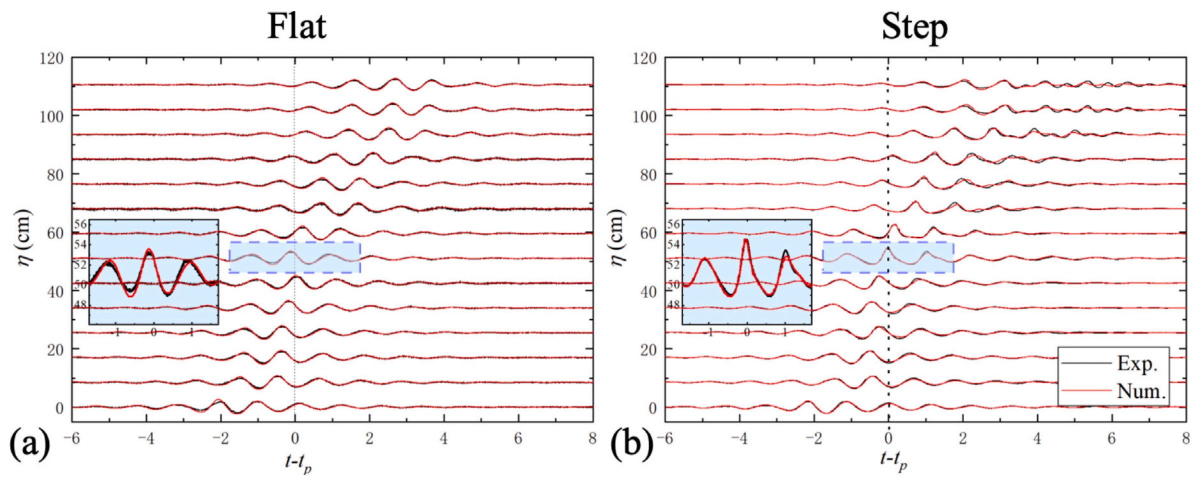

Fig. 3. Comparison of experimental measurements and numerical results for the surface elevation at the 14 wave gauge positions along the tank for Case 3 f_p = 0.9 Hz, k_pa = 0.08: (a) Flat and (b) Step conditions.

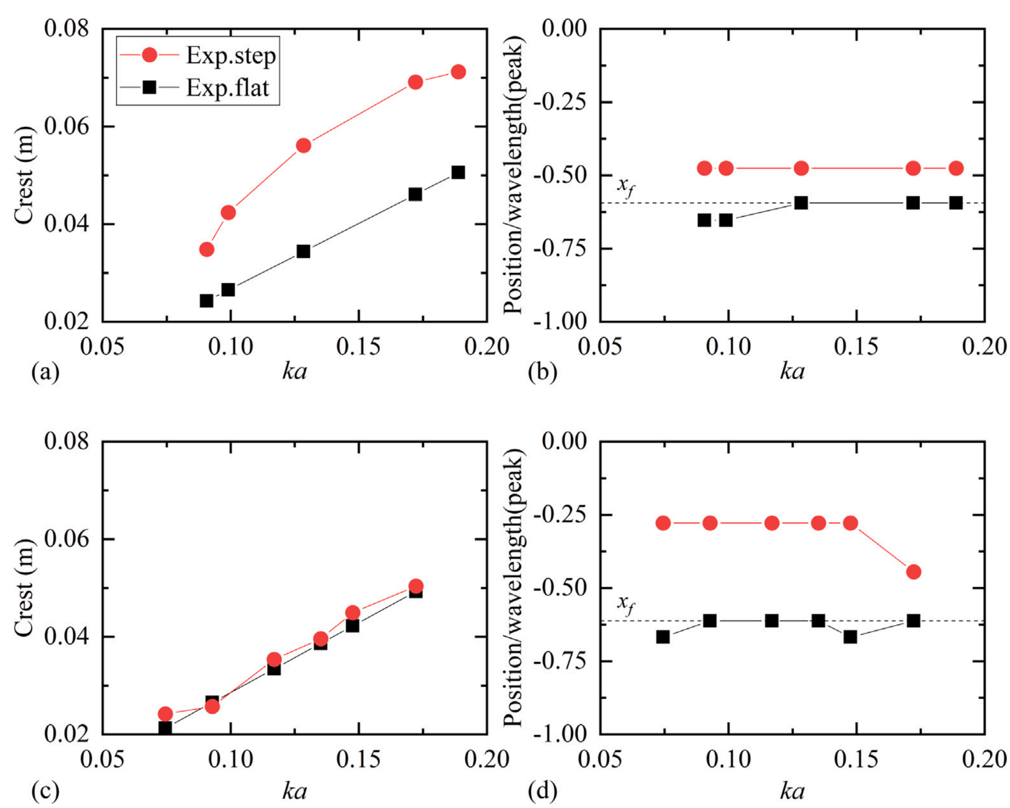

Fig. 4. (a) Maximum elevations of measured results in the case of h_d = 0.36 m, f_p = 0.9 Hz; (b) position of maximum elevations in the case of h_d = 0.36 m; (c) maximum elevations in the case of h_d = 0.48 m, f_p = 0.9 Hz; (d) position of maximum elevations in the case of h_d = 0.48 m. The results presented in all panels are based on laboratory observations.

To validate the accuracy of our numerical model, we compare the experimental measurements and numerical solutions for Cases 3 over flat and step conditions in Fig. 3. The experimental and numerical results agree well for two cases with capturing the wave characteristics during nonlinear propagation. For instance, at the focusing time, the crests become sharper over the rectangular step in Fig. 3(b). Notably, the main groups are followed by additional minor wave groups, corresponding to reflected waves caused by the rectangular step. Overall, the acceptable agreement across both bottom topographies (flat and stepped) validates our numerical model.

3. Results and discussion

The nonlinear propagation of focused wave groups over the rectangular step is examined from the perspective of both temporal and spatial domains. Specifically, the study focuses on wave crest characteristics, harmonic variations and kurtosis on deterministic signals. Section 3.1 presents the crests and their corresponding positions for various wave conditions. Section 3.2 illustrates the specific spatio-temporal evolution of the first four harmonics. Utilizing phase-manipulation techniques and CWT, the decomposition of superharmonics is achieved,

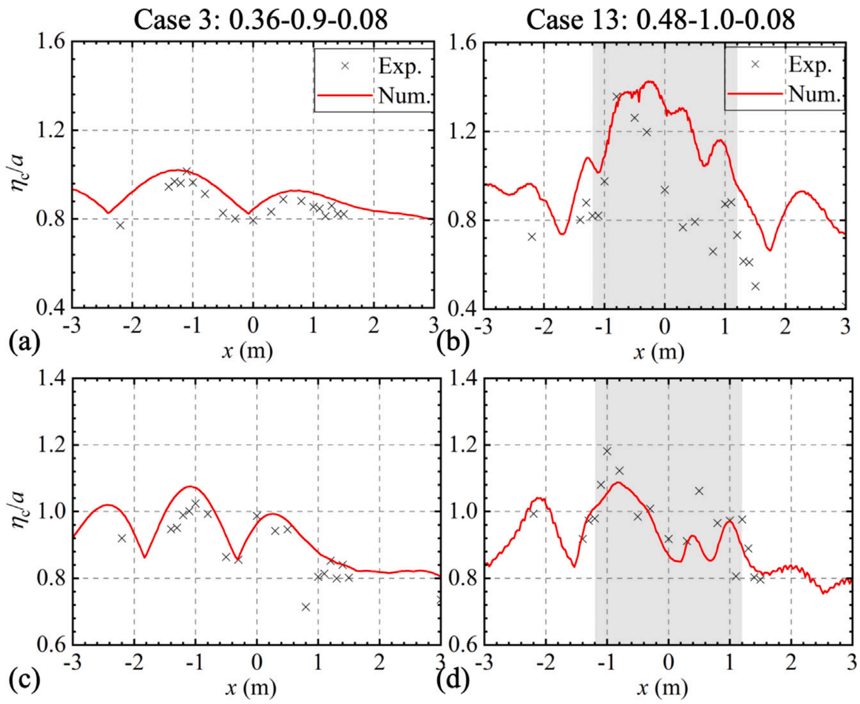

Fig. 5. Spatial variation of normalized crests with numerical (red solid line) and measured results (black crosses) in flat and step (shaded) conditions. The label denotes the water depth h_d, the peak frequency f_p and incident wave steepness k_pa, respectively.

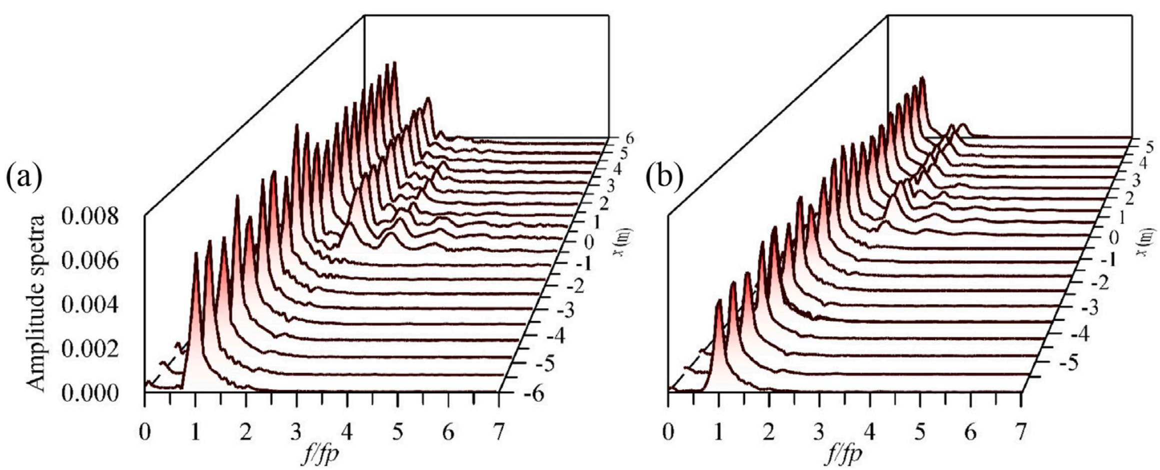

Fig. 6. Numerical solutions for the spatial evolution of wave spectrum harmonics along the rectangular step for (a) Case 1 and (b) Case 3.

along with the identification of higher bound and free waves. Section 3.3 presents the analysis of deterministic signals over the rectangular step.

3.1. Wave group crest

During pre-testing, the focusing positions for all cases have been prescribed at $x_f = -1.0$ m (WG 6) in flat seabed conditions, as seen in Fig. 4(b) and (d). Fig. 4 compares the wave crests and their locations for both flat and step seabeds at two different water depth conditions ($h_d = 0.36$ m and $h_d = 0.48$ m), with an incident peak frequency of 0.9 Hz. The horizontal axis shows the wave steepness. As illustrated in Figs. 4(a) and (c), the presence of a rectangular step results in significantly higher wave crests compared to flat seabed conditions, particularly when the water depth over the step is sufficiently shallow. In Fig. 4(a), the peak elevation increases from 0.024 m to 0.035 m for $k_pa = 0.08$, and from 0.046 m to 0.069 m for $k_pa = 0.17$. The growth rates are 40% for $k_pa = 0.08$ and 79% for $k_pa = 0.13$. In contrast, the case with deeper water depth $h_d = 0.48$ m exhibits a minor growth rate of about 4%, as depicted in Fig. 4(c). The position of crests shifts downstream depending on the step condition. For a water depth of $h_d = 0.36$ m, the peak occurs at $x = -0.8$ m (Fig. 4(b)), whereas for the deeper water depth $h_d = 0.48$ m, the shift is more pronounced at $x = -0.5$ m (Fig. 4(d)). In conclusion, the spatial lag increases from 0.12–0.18 peak wavelengths at $h_d = 0.36$ m to 0.28–0.39 peak wavelengths at $h_d = 0.48$ m.

Fig. 5 shows the normalized peak elevations along the tank for different test cases, with the rectangular step indicated by the shaded area. Both measured and numerical results are normalized by the maximum focal crest amplitude a over a flat seabed. The labeling convention, exemplified by "0.36-1.0-0.08" denoting $h_d = 0.36$ m, $f_p = 1.0$ Hz and $k_pa = 0.08$, respectively, is consistently used throughout the study. The numerical results capture the overall spatial evolution trend, showing good agreements in the flat scenarios. However, localized discrepancies

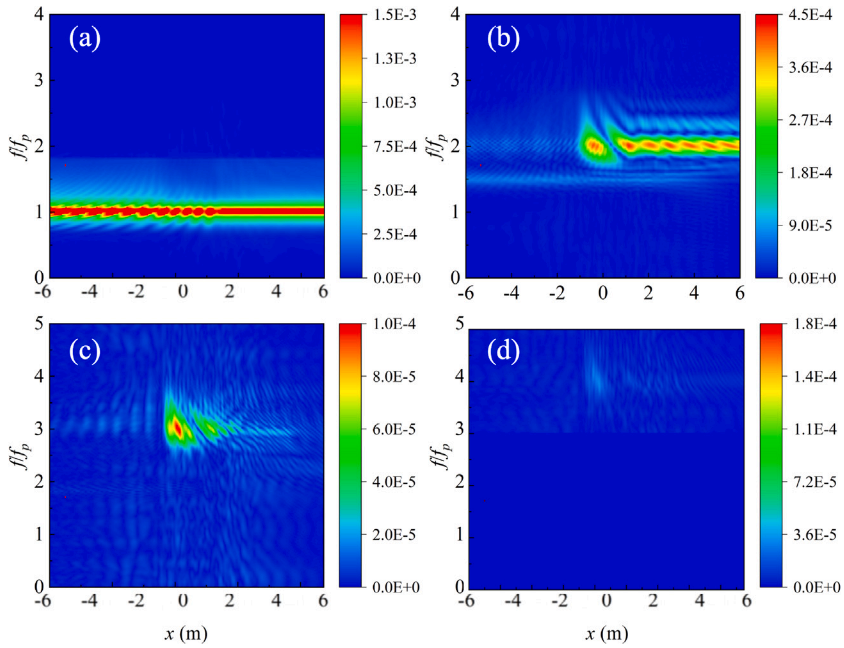

Fig. 7. Spatial evolution of the first four harmonics for Case 3.

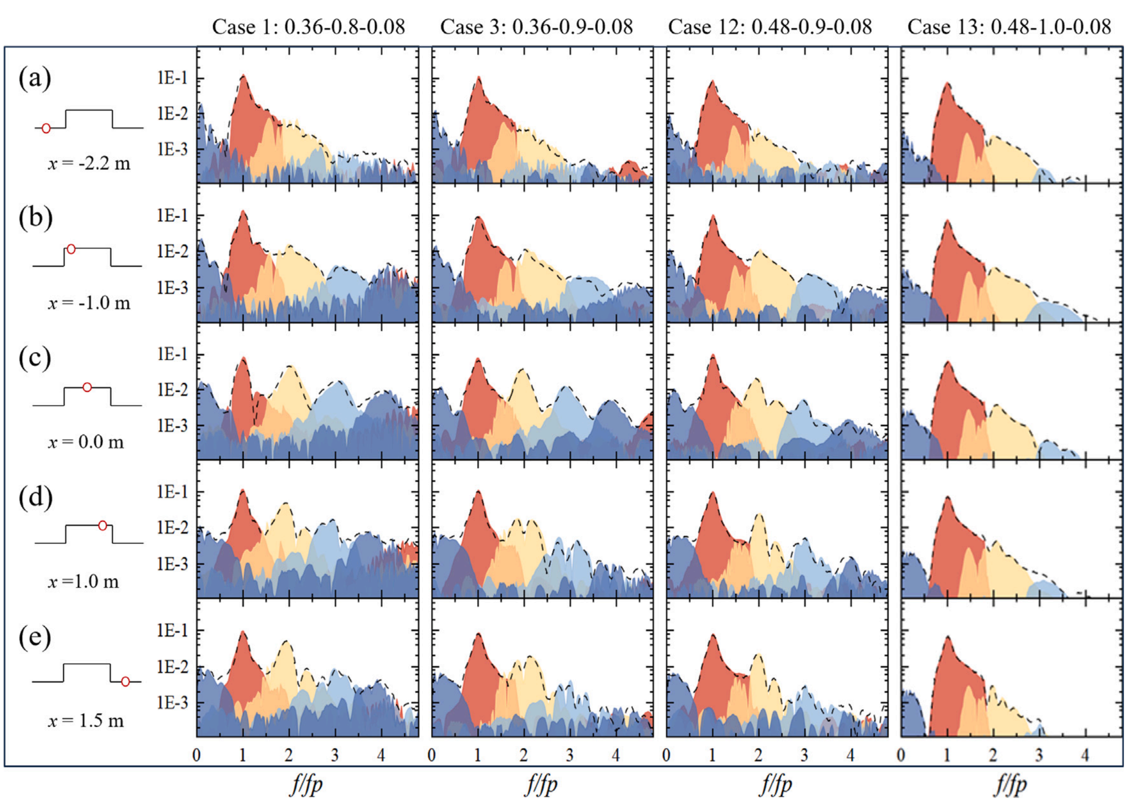

Fig. 8. Decomposed elevation spectra for four selected cases at five positions: (a) $x = -2.2$ m; (b) $x = -1.0$ m; (c) $x = 0.0$ m; (d) $x = 1.0$ m and (e) $x = 1.5$ m.

are observed at the peak elevations immediately downstream the step. This local deviation is primarily attributed to differences in the wave generation method (piston wavemaker in the experiment while spatial prescription in the numerical model), which introduces a slight spatial phase shift in the generated free waves. As further elucidated in Fig. 15, after extracting the free wave components, the spatial evolution of the bound harmonics for the numerics shows a good agreement with the measurements. The comparison between the measured and numerical results shows an acceptable qualitative agreement in maximum wave elevations for all cases.

Regarding the specific evolution pattern, the spatial evolution of the wave crest elevation shows a distinct pattern, beginning with a minor

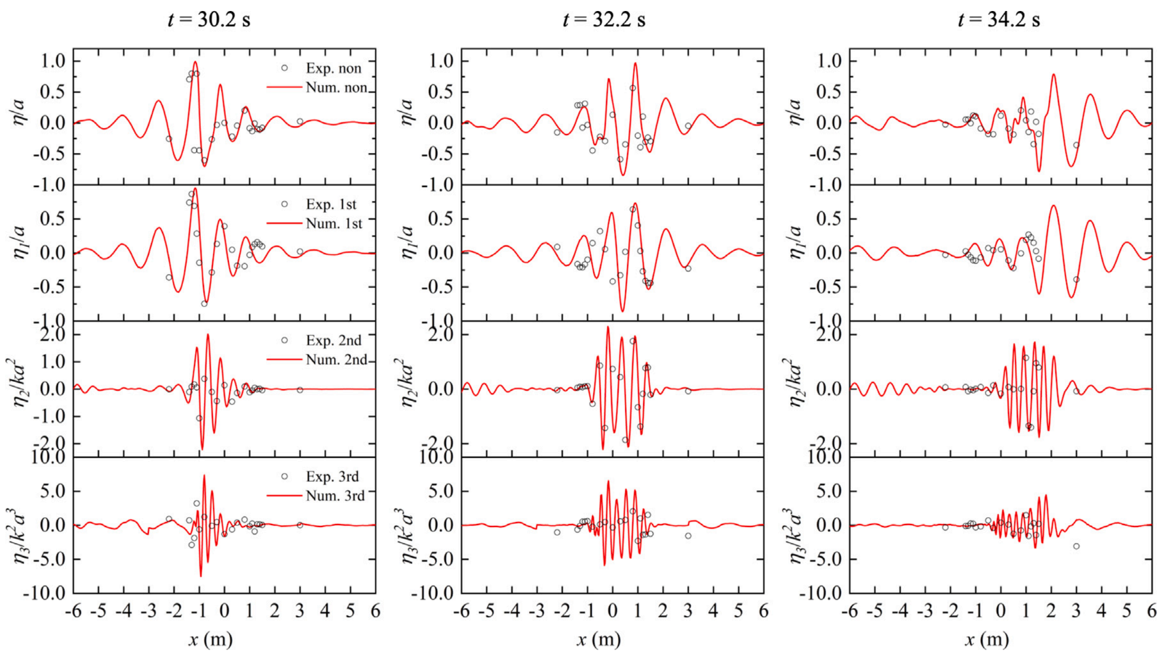

Fig. 9. Wave profiles of decomposed harmonics at selected time instants for Case 7.

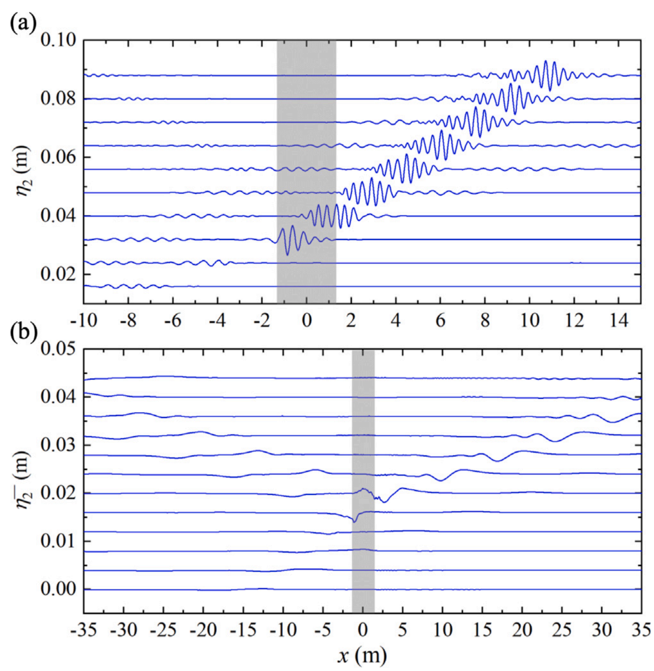

Fig. 10. Propagation of second superharmonics and subharmonics for Case 7.

decrease immediately upstream of the first depth change. From this position, elevations gradually increase to reach their maxima around $x = -1.0$ m before declining steadily until encountering the second depth change at $x = 1.2$ m, where another local increase occurs. Downstream of the step, wave crests stabilize to nearly constant values. The comparison between the two relative water depths reveals that the crest amplification over the step is less pronounced for $h_d = 0.48$ m than for $h_d = 0.36$ m. This difference suggests that wave group interactions with the rectangular step become progressively weaker with increasing relative water depth, highlighting the important role of $k_p h_d$ in governing wave transformation processes.

3.2. Superharmonics evolution

This section presents a detailed harmonic analysis, examining the evolution of both fundamental and superharmonic components in temporal and spatial domains. Section 3.2.1 discusses the spatial propagation of individual harmonics, revealing their evolutionary patterns and spectral characteristics at selected positions. Then, Section 3.2.2 shows the application of the phase method (introduced in Appendix B) to separate superimposed superharmonic components, providing clear identification of each superharmonic. For analyzing second-order free and bound waves sharing identical frequencies, the section illustrates how the wavelet transform overcomes the limitations of Fast Fourier Transform by providing time–frequency resolution, with results presented in Section 3.2.3.

3.2.1. Spectral evolution

Fig. 6 presents the spectral variations for Cases 1 and 3, showing the fundamental component peaking at $x = -1.0$ m, followed by the emergence of second and third harmonics. Along the tank, each wave component diminishes at the second depth change ($x = 1.2$ m). However, the specific propagation distance and spatial decay rate of the third harmonics vary noticeably depending on the incident wave frequency. Furthermore, the distinct spatial variations in spectral amplitudes observed upstream of the step are a direct consequence of wave reflection (as well as in Fig. 7). The interference between the backwards-propagating components (illustrated in Fig. 10) and the incoming incident waves forms a partial standing wave field, causing the observed spatial modulation of harmonic amplitudes.

3.2.2. Superharmonics

A phase-manipulation approach, specifically the four-phase-based method, has been utilized to extract superharmonics from the elevations of focused waves. This approach is particularly useful for analyzing focused wave groups where overlapping of harmonics is expected and the simple FFT is not effective. Detailed descriptions for this method are presented in Appendix B. Fig. 7 illustrates the first four harmonics extracted in the spatial domain for Case 3, which features an incident frequency bandwidth $f/f_p \in [0.3, 1.8]$. Note that different color scales are adopted to clearly present each harmonic. For the first harmonic in Fig. 7(a), small fluctuations are observed

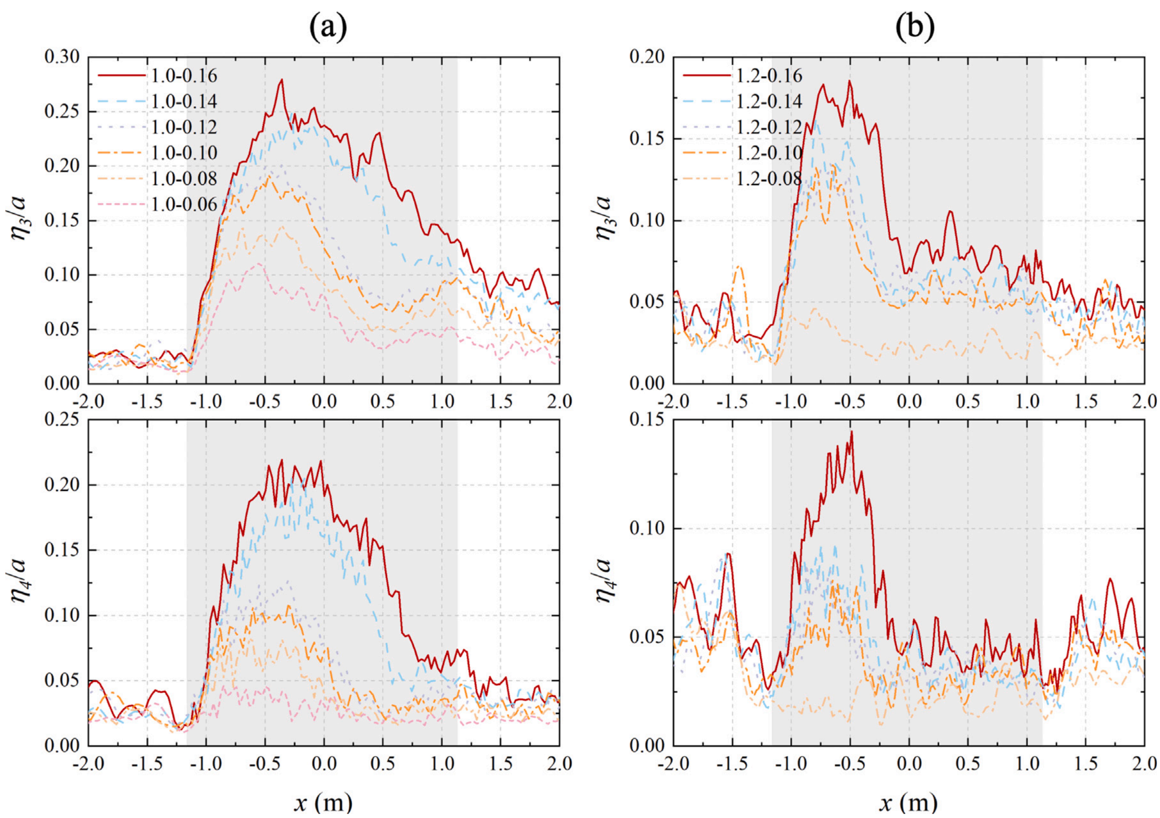

Fig. 11. Spatial variation of third and fourth harmonics at (a) $f_p = 1.0$ Hz, $h_d = 0.36$ m and (b) $f_p = 1.2$ Hz, $h_d = 0.36$ m. The legend format follows "f_p - $k_p a$", representing the incident peak frequency and wave steepness, respectively.

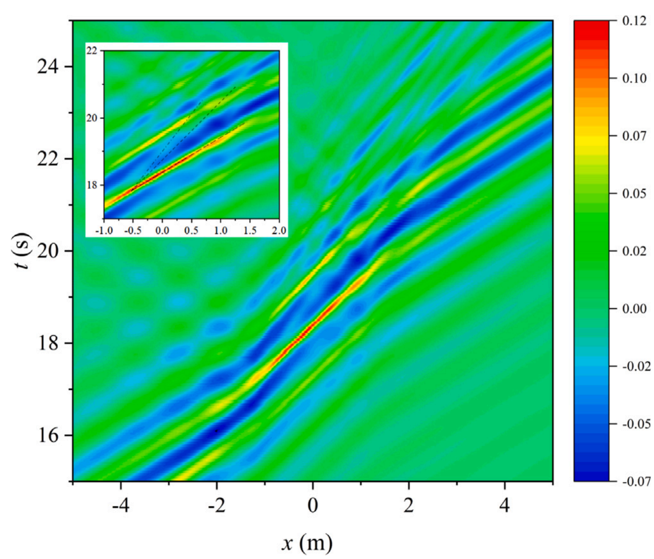

Fig. 12. Spatio-temporal representation of focused wave groups for Case 3.

when the group propagates through the rectangular step. The second harmonic is clearly induced at $x = -1.0$ m (Fig. 7(b)), at the focusing position on the step, with a frequency bandwidth approximately $f/f_p \in [1.8, 2.6]$, which narrows as it passes through the rectangular step. A distinct spatial beating pattern is observed in the second harmonic evolution, which manifests as alternating nodes and antinodes. This beating behavior arises from the interference between the phase-locked bound waves and the bathymetry-induced free waves propagating at different celerities. Additionally, components of the third harmonic in Fig. 7(c) and the fourth harmonic in Fig. 7(d) are visible, with the fourth harmonic being nearly zero. The FFT method is limited by its inability to resolve overlapping frequency components. Fig. 7 demonstrates the effectiveness of the phase manipulation method in isolating individual harmonics, offering a more accurate representation of harmonic evolution in focused wave groups.

The decomposed spectra at five different locations for four selected cases are presented in Fig. 8, with numerical results indicated by colored areas and experimental data by black dotted lines. The surface elevations have been normalized with the crest a obtained in constant water depth. In the step condition with $h_d = 0.36$ m, the amplitudes of the first to fourth harmonic components are higher compared to the case with $h_d = 0.48$ m. Due to overlap between harmonic components, four distinct colors are used to distinguish each harmonic. The results show that the peak amplitude of each harmonic decreases with increasing order, and superharmonics are more pronounced for smaller $k_p h_d$. For instance, in Case 3 at $x = -1.0$ m, the fundamental and second harmonic peaks are approximately 0.15 and 0.02, respectively. As the wave group propagates to $x = 0.0$ m, the frequency range of each harmonic narrows, and the peak of the fundamental decreases to 0.1, with subsequent harmonics also reduced. A notable observation is the sudden drop occurring only in the second harmonic, indicating that this feature is associated with the frequency component near the second harmonic rather than a superposition of multiple harmonics. Overall, the phase-manipulation method enables clear extraction and visualization of the evolution of each harmonic component along the propagation path.

Fig. 9 presents the decomposed wave profiles with both measured and numerical results. The maximum amplitude of each harmonic is normalized with the wave steepness as $\eta_n/(k_p^{n-1}a^n)$ for all cases. The amplitudes of fundamental harmonics reach their maxima approximately at $t = 30.2$ s. Subsequently, the crests of fundamental components decrease gradually, but those of superharmonics increase

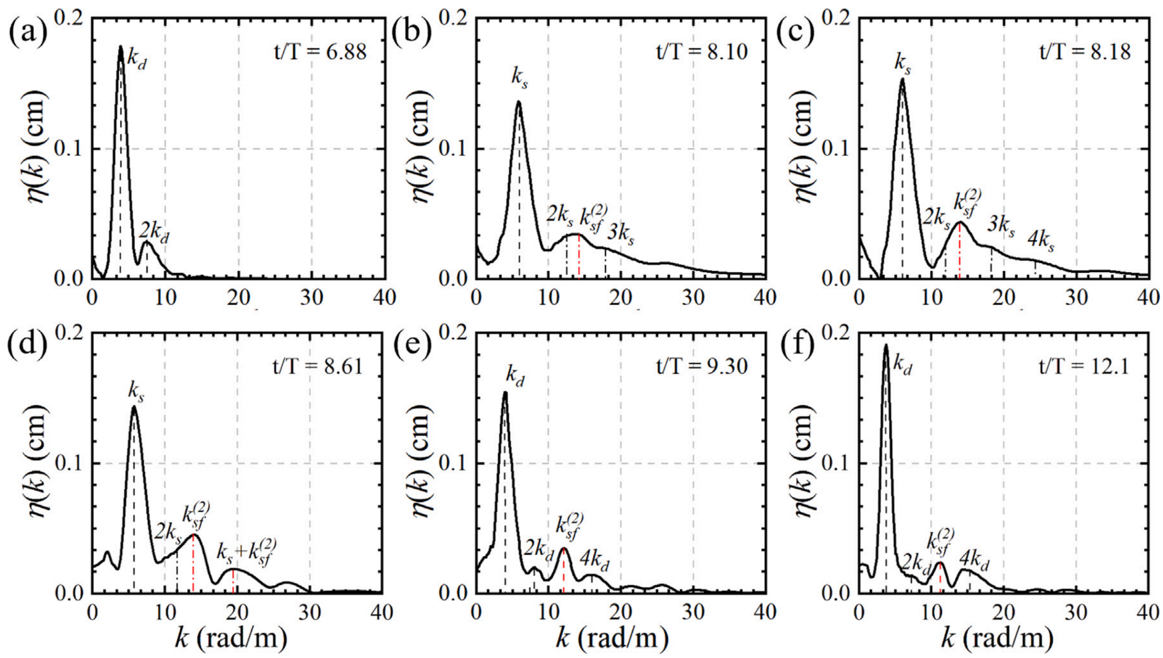

Fig. 13. Numerical results of the spatial Fourier amplitudes at the local spectral peaks (denoted as peak amplitude $\eta(k)$) for Case 3, as a function of wavenumber at six time instants: (a) $t/T = 6.88$; (b) $t/T = 8.10$; (c) $t/T = 8.18$; (d) $t/T = 8.61$; (e) $t/T = 9.30$ and (f) $t/T = 12.1$.

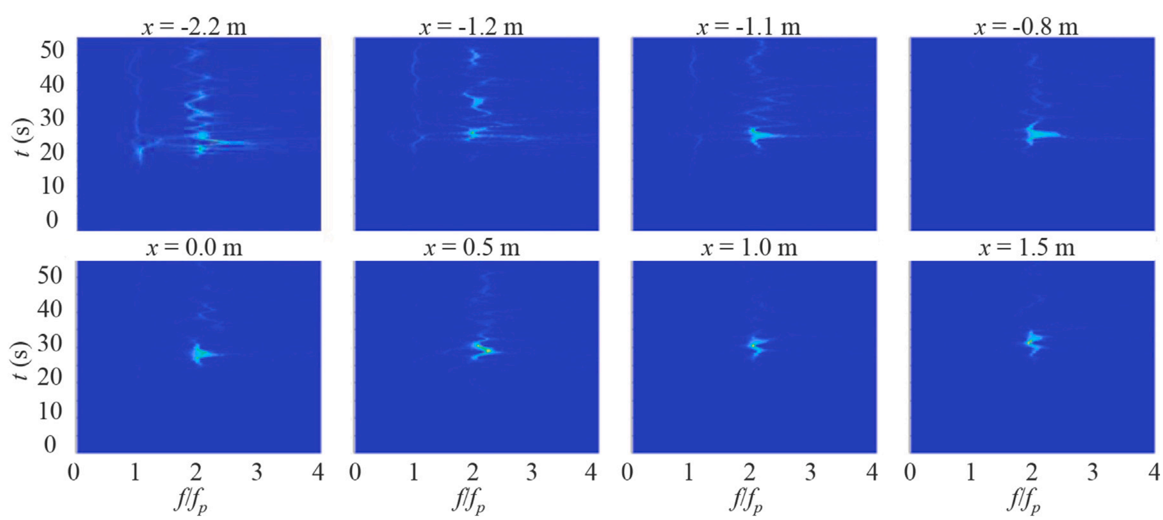

Fig. 14. Temporal variation of second harmonics for Case 3 for selected positions.

after propagating over the first depth change. Two successive crests of second harmonics can be found over the step starting from t = 32.2 s. In addition, the length of the envelope of the second harmonics becomes longer at t = 34.2 s since the phase velocities of the second-order bound and free waves are different. Furthermore, Fig. 10 presents the numerical solutions for second harmonic η_2 and subharmonic generation η_2^-. The second harmonics first emerge at the first depth change position. During propagation of the focused wave groups along the tank, a second-order free wave component develops and trails the second-order bound wave. A distinct second harmonic component is also observed in the reflected wave field, propagating in the opposing direction. The subharmonic components η_2^-, exhibiting long-wave characteristics, manifest through variations in the mean water level (Janssen et al., 2003). These low-frequency waves originate at the first depth change and possess significantly longer wavelengths and higher phase velocities than those associated with superharmonic components. Consequently, during the nonlinear propagation of focused wave groups over an abrupt depth change, the second-order wave field can be decomposed into superharmonic and subharmonic bands. Upon encountering the step, each band splits into a complex superposition of transmitted and reflected waves, encompassing both bound and newly generated free harmonics. Such a multi-component propagation further demonstrates the crucial importance of accurate harmonic separation for a comprehensive understanding of the wave transformation.

In addition to the second harmonics, we examine the influence of wave steepness k_pa on the third and fourth harmonics. For cases with f_p = 1.0 and 1.2 Hz, Fig. 11 displays the spatial evolution of third and fourth harmonic amplitudes. The results demonstrate that increased wave steepness k_pa leads to larger superharmonic amplitudes in shallower regions, while also causing a downstream shift in their peak positions. Furthermore, the growth of peak amplitudes exhibits a nonlinear pattern, where successive increases in wave steepness result

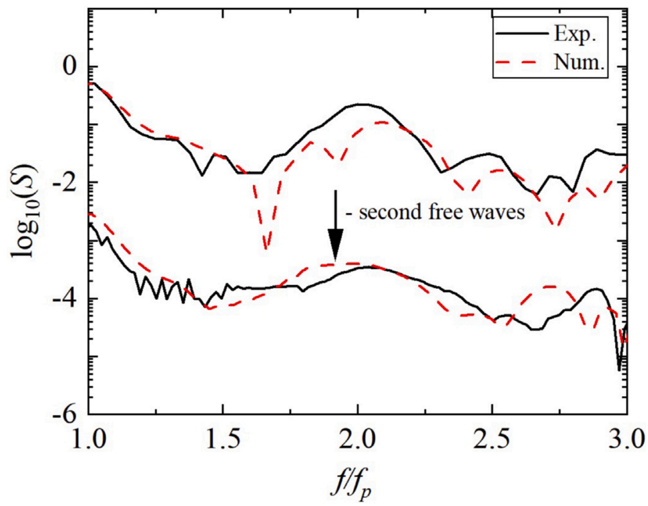

Fig. 15. The wave spectra for Case 3 (WG 14) with and without the second-order free waves.

in progressively smaller increments in peak magnitude. Crucially, the delayed generation and downstream spatial shift of these individual third and fourth harmonic peaks directly drive the overall downstream shift of the actual wave group focusing position. These superharmonics (third and fourth) significantly influence the shape of wave crests. Therefore, accounting for the effects of superharmonics is essential for the accurate modeling and prediction of wave behavior in coastal and offshore engineering applications.

3.2.3. Second-order free and bound waves

To comprehensively investigate the existence of free waves, we analyze these waves from two distinct perspectives. The Ursell number serves as a dimensionless parameter characterizing wave nonlinearity. For Case 3, the nondimensional wavenumber $k_d h_s = 0.45$ corresponds to pronounced nonlinearity, with $U_r = 84$. As suggested by Monsalve et al. (2015), it is the interaction of such a highly nonlinear wave field with the abrupt bathymetric transition that causes the significant release of second-order free waves. The spatio-temporal representation of the numerical surface elevations for Case 3 (Fig. 12) provides evidence of second-order free waves. Phase velocities were directly extracted from the spatial–temporal slopes ($\Delta x/\Delta t$) of the wave trajectories. The three distinct values of these slopes confirm the presence of fundamental, second- and third-order free wave components. As detailed in the localized inset of Fig. 12, faint but distinct wave striations emerge parallel to the steeper dashed guidelines, confirming the generation and slower propagation of the second- and third-order free waves. The measured phase velocities of these three free components are 0.99, 0.68, and 0.57 m/s, respectively. These measurements align closely with theoretical predictions from the dispersion relation (0.94, 0.75, and 0.53 m/s for the first three harmonics). This strong agreement between the slope-extracted and theoretical velocities provides robust evidence for the presence of higher-order free waves, while the large U_r explains the mechanism behind their significant generation over the step.

Based on the dispersion relation, the wavenumber spectrum effectively distinguishes between free and bound waves. Fig. 13 illustrates the spatial evolution of the wavenumber spectrum at six temporal instants. The analysis was conducted within a frequency range of 0.3 to 1.8 times the primary frequency, a selection optimized for the separation of superharmonics. In the deeper region (Fig. 13(a), $t/T = 6.88$), two spectral peaks are observed: the dominant peak corresponds to the fundamental bound wave at $k_d = 3.9$ rad/m, associated with the focused wave group propagating ahead of the step, while a second peak at $2k_d$ is identified as the second-order bound wave. The component labeled $k_{sf}^{(2)}$ in shallower regions is attributed to a second-order free wave. As the wave group traverses the first depth change at $t/T = 8.10$, the primary wavenumber shifts to $k_s = 5.96$ rad/m, consistent with changes in the linear dispersion relation due to decreasing water depth. At this stage, over the depth change, both the second-order bound wave ($2k_s = 11.92$ rad/m) and the second-order free wave ($k_{sf}^{(2)} = 13.90$ rad/m) become apparent. Furthermore, nonlinear wave–wave interactions during the evolution of the focused wave and its coupling with the bathymetry generate additional higher components, evident as third ($3k_s$) and fourth ($4k_s$) harmonic components.

By $t/T = 8.61$, as the wave groups propagate across the middle of the step, three distinct spectral maxima emerge: (1) the fundamental free wave component at k_s, (2) the second-order free wave at $k_{sf}^{(2)}$, and (3) a component at ($k_s + k_{sf}^{(2)}$), tentatively identified as a sum–frequency interaction product between the first and second-order free harmonics (Monsalve et al., 2022). Subsequently, at $t/T = 8.18$, the amplitude of free wave components increases significantly, exceeding those of the bound waves. This trend highlights the growing dominance of second-order free waves in the shallower regions following the first depth change. Finally, by $t/T = 9.30$, after the wave groups have traversed the rectangular step, the bound wave amplitudes decay to negligible levels (approximately 0.02 cm), significantly smaller than those of the second-order free waves. These observations, based on the distinct wavenumber signatures, demonstrate the presence and evolution of free waves. They further highlight the critical role of free waves in amplifying the second harmonics, particularly at the second depth change.

Since the frequency ranges of second-order bound and free waves overlap, the CWT is applied to distinguish them in the time domain, presented in Appendix C. Fig. 14 presents the variation of second harmonics, with the horizontal axis representing normalized frequency and the vertical axis indicating time. At WG 5 ($x = -1.1$ m), distinct second harmonics appear near the focusing time $t_f = 30$ s. Around WG 12 ($x = 0.5$ m), located downstream of the central step, a separation in the second harmonics becomes evident. This separation is driven by the different group velocities of the bound and free components, which cause them to arrive at the measurement location at different times. The temporal evolution of frequencies reveals two local maxima: one at $t = 30.2$ s for the bound waves and another at $t = 31.5$ s for the free waves. Furthermore, the partial overlap and interference between these temporally shifted packets cause the observed spreading and splitting around the central frequency band. The discrepancies in second harmonic components between experimental and numerical results are likely attributable to differences in wave generation methods and wavemaker-to-focus distances. While these factors introduce phase differences in free wave generation, they do not significantly influence the analysis of spatial evolution characteristics of harmonic components.

The second harmonics in wave spectra, with and without the second-order free waves, are compared in Fig. 15 for Case 3 at $x = 1.0$ m (WG 14). Crucially, upon removal of the second-order free wave, the abrupt drop in the spectral magnitude disappears in both the experimental and numerical results, yielding a smoother and lower-energy profile. This finding further substantiates that the superposition of the second-order bound and free waves leads to a sudden decrease in the wave spectrum. Additionally, this abrupt harmonic drop, caused by the interaction of the second-order bound and free wave, can also serve as an indicator of the presence of a second-order free wave. Fig. 16 presents the spatial evolution of the maximum elevations of separated second-order bound and free waves for Cases 7 and 9. The generation of second-order bound waves is found at the first depth change, reaching a maximum amplitude downstream of the focusing position at $x = -0.9$ m. A minor amplitude peak is observed near $x = 1.0$ m following the second depth change. Beyond the step, the peak amplitudes of bound waves attenuate and eventually stabilize. In

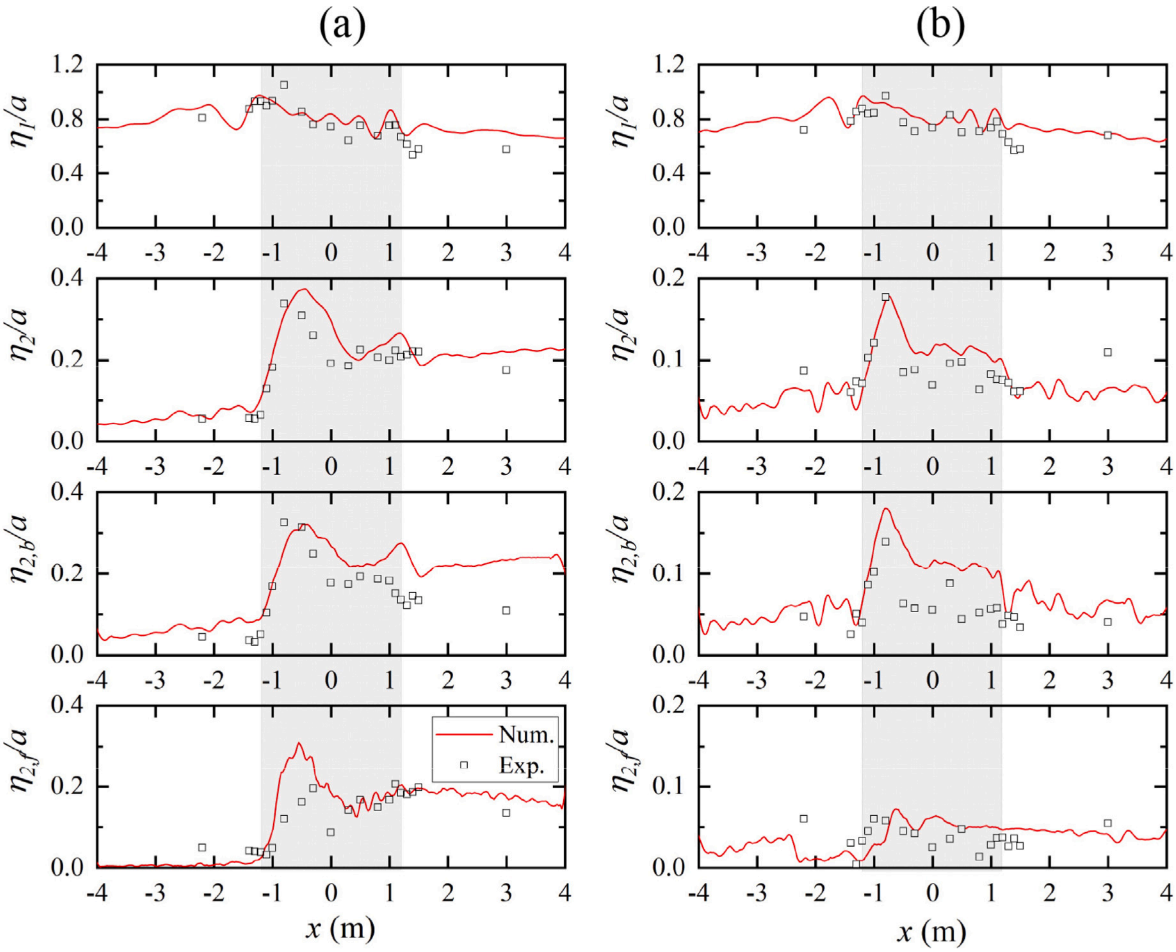

Fig. 16. Spatial variation of second-order bound and free waves for (a) Cases 7 and (b) Case 9. The notations $\eta_{2,b}$ and $\eta_{2,f}$ represent the maximum surface elevations of the second-order bound and free waves, respectively, while η_1 and η_2 denote the fundamental wave and the total second harmonic.

contrast, the crest positions of free waves remain largely consistent with those of bound waves but exhibit lower amplitudes. A single increase in amplitude is observed in the shallower region. Unlike the abrupt amplification of bound waves at the second depth change, the free waves display a more gradual variation in amplitude. Notably, downstream of the step, the peak crests of free waves surpass those of bound waves. While linear dispersion conserves the total spectral energy of the free wave group, the differing group celerities of its constituent frequencies cause the packet to elongate spatially. As the conserved energy is distributed over a continuously widening area, the local maximum envelope amplitude naturally decays (Mei, 1989). These observations highlight distinct mechanisms for second harmonic enhancement at the two depth changes, with free waves playing a dominant role at the second depth change.

3.3. Analysis of deterministic signals

To quantitatively evaluate the nonlinear deformation of the wave profile, the third-order moment (λ_3) and the fourth-order moment (λ_4) of the surface elevation are calculated. These parameters correspond to the skewness and kurtosis of the deterministic wave field, respectively. For a discrete wave elevation time series $\eta(t)$, these indices are defined as follows:

$$\lambda_3 = \frac{\frac{1}{n}\sum_{i=1}^{n}(\eta_i - \bar{\eta})^3}{\left(\sqrt{\frac{1}{n}\sum_{i=1}^{n}(\eta_i - \bar{\eta})^2}\right)^3}, \tag{12}$$

$$\lambda_4 = \frac{\frac{1}{n}\sum_{i=1}^{n}(\eta_i - \bar{\eta})^4}{\left(\frac{1}{n}\sum_{i=1}^{n}(\eta_i - \bar{\eta})^2\right)^2}, \tag{13}$$

where n is the total number of data points in the time series, and $\bar{\eta}$ denotes the mean surface elevation. As shown in Fig. 17, in the flat seabed, the λ_3 remains are near zero across the entire domain, while the λ_4 peaks at $x = -1.0$ m near $\lambda_4 = 10$, corresponding to the prescribed wave focusing position. The introduction of a submerged step leads to increases in both λ_3 and λ_4, reaching values of up to 1.4 and 14.2, respectively. Furthermore, the locations of these maxima are shifted downstream relative to the flat seabed case. Considering the spatial variation of harmonics in Fig. 11, the position of the peak λ_4 coincides with the appearance of the superharmonic. This observation suggests that the presence of the rectangular step leads to the generation of superharmonics, thereby enhancing skewness and kurtosis.

The influence of individual wave harmonics on skewness and kurtosis is analyzed via their superposition (Fig. 18). The fundamental harmonic shows similar behavior under step and flat seabed conditions (in Fig. 17(b)) but with a reduced crest sharpness parameter. Incorporating superharmonics, specifically the second-, third- and fourth-order bound components, amplifies the peaks of λ_3 and λ_4, particularly in shallower regions. However, the peak values of λ_3 and λ_4 obtained from this four-harmonic superposition are actually larger than those of the full, original nonlinear wave profile. This overestimation is corrected upon the inclusion of the second subharmonics (difference frequencies). The subharmonic components induce a local rise in the mean water level, which inherently weakens the morphological deformation of the wave profile. Consequently, this leads to a reduction in skewness and kurtosis. The superposition of harmonics demonstrates two nonlinearity mechanisms over step topography: superharmonic generation and mean waterline uplift. While superharmonics and subharmonics have

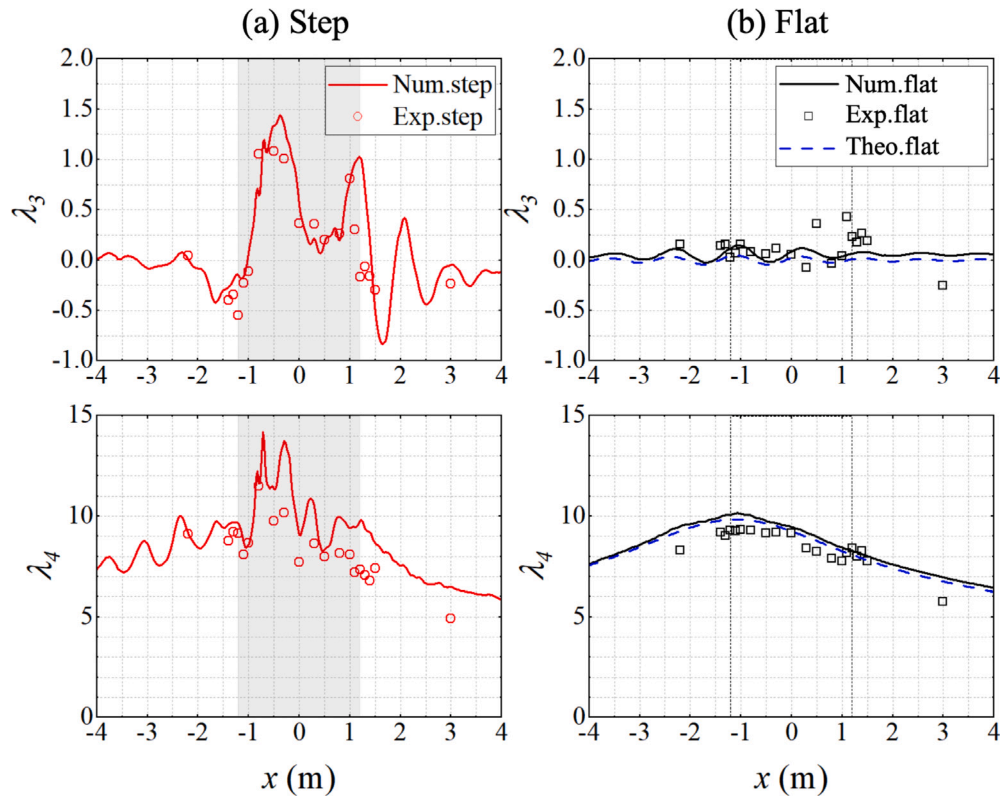

Fig. 17. Spatial variation of skewness and kurtosis in step and flat seabed conditions for Case 7. The curves labeled "Theo. flat" denote the corresponding theoretical values over a constant water depth.

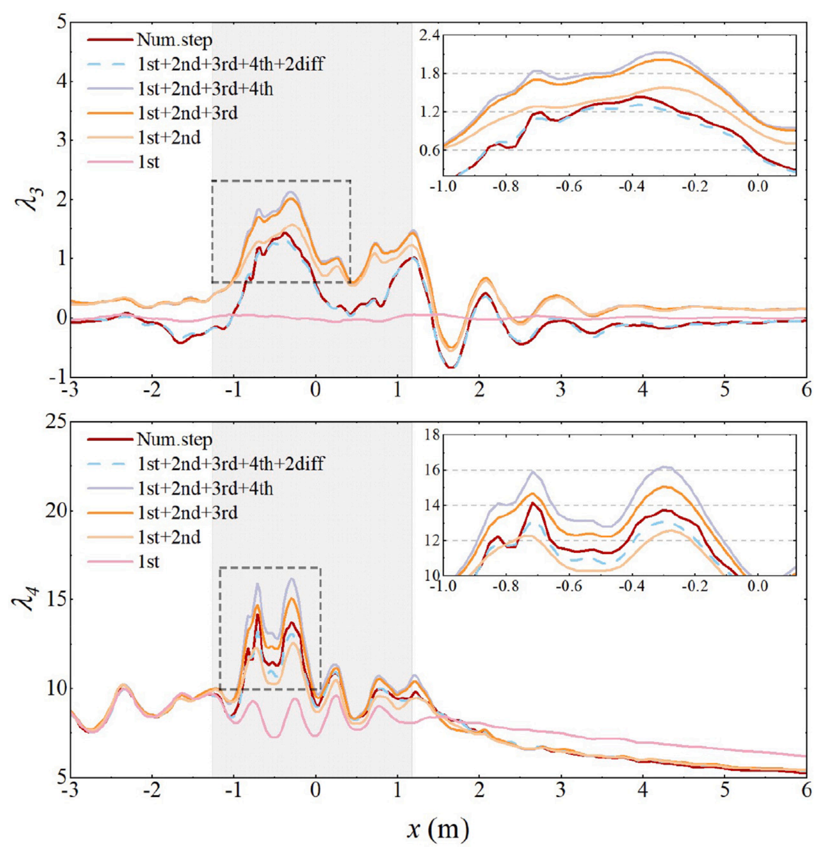

Fig. 18. Wave skewness (λ_3) and kurtosis (λ_4) with the superposition of superharmonics in the spatial domain for Case 7.

an opposite effect on spatial-domain skewness and kurtosis, the step topography elevates the overall λ_4 values. To conclude, the rise in the skewness (λ_3) indicates that the wave profiles become sharper, developing steeper crests and flatter troughs as they propagate over the step. Simultaneously, the enhancement of the crest sharpness parameter (λ_4) directly reflects the nonlinear wave steepening process, where wave energy is concentrated into a narrower region around the crest, leading to more extreme wave forms. These changes in wave morphology are physically linked to the generation of superharmonics discussed in Section 3.2.

4. Conclusions

This study investigates the evolution of focused wave groups propagating over a rectangular step through an integrated experimental and numerical approach. The research provides new insights into the complex nonlinear dynamics governing wave transformation over abrupt depth changes, with particular emphasis on superharmonic generation and evolution. The combined methodology of phase-manipulation technique and continuous wavelet transform analysis has proven highly effective in achieving precise spatio-temporal separation of superharmonic components. This approach has successfully enabled the identification and tracking of individual harmonic evolution, providing clear evidence of distinct spatial patterns between second-order bound and free waves. The characteristic frequency signatures resulting from wave superposition offer a novel indicator for free-wave detection in experimental studies.

The rectangular step induces substantial nonlinear energy transfer to higher-harmonic components, with the third and fourth harmonics exhibiting particularly enhanced crests in shallower regions. This amplification mechanism might be crucial for the accurate prediction of extreme wave characteristics in coastal areas with abrupt depth variations. A key finding concerns the systematic modification of wave focusing characteristics due to nonlinear interactions. In this study, the prescribed focusing position ($x_f = -1.0$ m) is located atop the rectangular step. The generation of superharmonics behind the initial focusing position causes a consistent downstream shift of the wave focusing location, while simultaneously enhancing wave crests through nonlinear interaction effects. This displacement phenomenon, which increases with increasing incident wave steepness, demonstrates the coupled influence of topography and nonlinearity on wave group dynamics. The pronounced enhancement of both skewness and kurtosis on deterministic signals provides direct evidence of nonlinear energy transfer processes, offering comprehensive explanations for the observed waveform deformations.

The identified migration of extreme wave energy induced by the rectangular step potentially increases coastal hazard, particularly in regions with similar abrupt bathymetric variations. These findings highlight the critical importance of incorporating nonlinear wave dynamics and detailed bathymetric features into coastal vulnerability assessments. The methodologies developed and physical insights gained from this study establish a foundation for improved prediction of extreme wave events and support the development of enhanced coastal management strategies in complex nearshore environments.

CRediT authorship contribution statement

Qian Wu: Writing – original draft, Software, Methodology, Investigation, Formal analysis, Conceptualization. **Xingya Feng:** Writing – review & editing, Supervision, Methodology, Investigation, Conceptualization. **You Dong:** Writing – review & editing, Methodology, Investigation, Conceptualization. **Wooyoung Choi:** Writing – review & editing, Methodology, Investigation, Conceptualization. **Frédéric Dias:** Writing – review & editing, Supervision, Methodology, Conceptualization.

Acknowledgments

Q.W. and X.F. show gratitude to the sponsorship provided by the National Key Research and Development Program of China (Grant No. 2023YFB3711500). Q.W. also acknowledges the financial support of the Research Grants Council of Hong Kong (TRS #T22-607/24-N) and the State Key Laboratory of Climate Resilience for Coastal Cities (ITC-SKLCRCC26EG01).

Declaration of competing interest

The authors declare that they have no known competing financial interests or personal relationships that could have appeared to influence the work reported in this paper.

Appendix A. Model convergence

As mentioned in Section 2.1, the conditions are set with $t_f = 30$ s and $x_f = -1.0$ m, the frequency bandwidth $f/f_p \in [0.3, 1.8]$, the middle position of the step is at $x = 0.0$ m and the length of the rectangle is 2.4 m. The numerical tank is designed to be 60 peak wavelengths long. This length minimizes wave reflection and allows for the complete propagation of the longest wave component.

In the numerical model, the choice of an optimum number of grid points (equivalently the number of Fourier modes) is crucial for accurate simulations. If the number of grid points is too small or too large, the computation can be inaccurate or too time-consuming. To evaluate the convergence of our numerical model, we vary the number of grid points per peak wavelength, ranging from 20 to 90, primarily focusing on cases involving a rectangular step. Fig. A.19 shows the surface profiles for different spatial resolutions and the amplitudes of second and third harmonics at the focusing time for Case 4. It is found that, except for a small discrepancy near the highest peak, the computed wave profiles are insensitive to the number of grid points if the number of grid points per wavelength is greater than 30, as shown in Fig. A.19(a). The amplitudes of the second and third harmonics are extracted using FFT, and compared with the results with 50 points per wavelength. The results indicate that the second harmonics converge at 50 points, while the third harmonics show minimal discrepancies beyond 40 points. Therefore, a resolution of 50 points per wavelength was selected for all subsequent simulations. This choice represents a computationally efficient compromise that ensures the convergence of key harmonics critical to this study, as evidenced by the negligible differences observed with higher resolutions (e.g., 90 points).

To quantify the morphological deformation of the deterministic wave profiles, we calculate two waveform parameters corresponding to skewness and kurtosis. The skewness (third-order moment, λ_3) measures the relative deviation of the wave profile from the mean water level, specifically characterizing the physical distinction between sharp, elevated crests and flat, shallow troughs. These parameters are computed using the same mathematical definitions as the statistical skewness and kurtosis, but here they serve as quantitative descriptors for a single wave event's shape, not as statistical moments of a random dataset. The influence of the number of grid points on skewness (λ_3) and kurtosis (λ_4) is also analyzed, as shown in Fig. A.20. The results reveal that the λ_4 converges to a value of 8.5 when the number of discrete points exceeds 30. Since the λ_3 of linear focused wave profiles is nearly zero (discussed in Section 3.3), the value remains small and fluctuates around -0.2 for different grid points. It is noted that at extremely fine grid resolutions (e.g., significantly beyond 40 grid points per wavelength), a slight deviation from the convergence trend is observed, which is primarily attributed to the accumulation of high-frequency numerical noise. Nevertheless, robust convergence is confirmed at the selected optimal resolution, ensuring the numerical reliability of the simulated results. In this study, we use 50 grid points per wavelength in the numerical simulations.

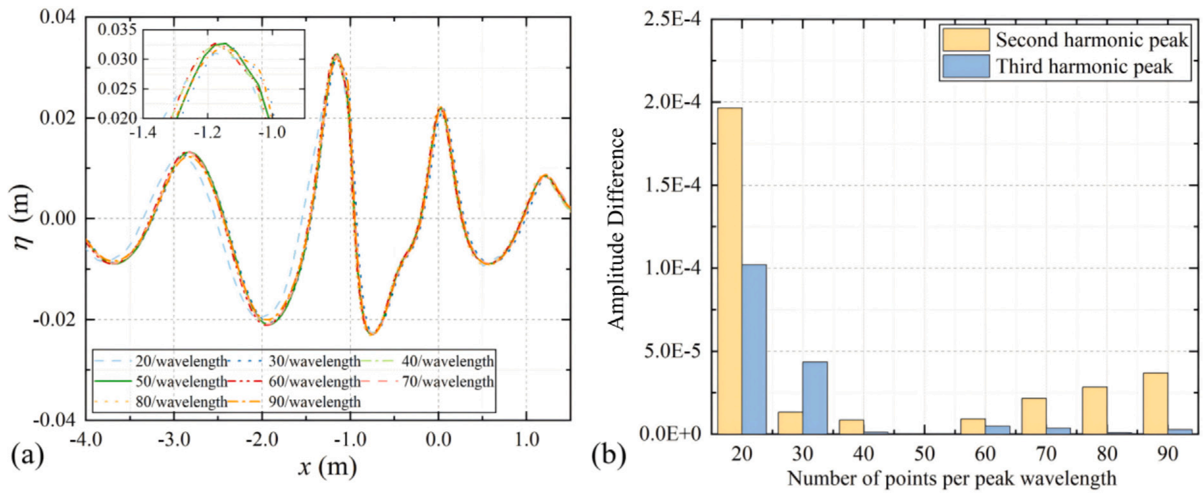

Fig. A.19. Convergence of the numerical model for Case 4 with different grid points per wavelength: (a) wave profiles with different grid points per wavelength and (b) Difference between harmonic amplitudes for various grid points per wavelength and those for 50 grid points per wavelength.

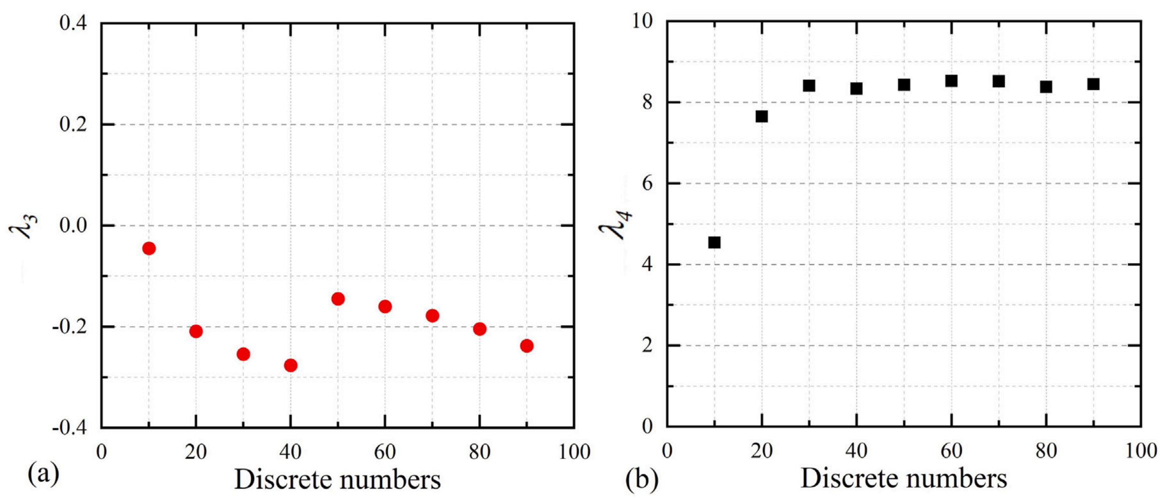

Fig. A.20. Convergence of numerical model for Case 4 with different grid points per wavelength: (a) skewness (λ_3) on rectangular step and (b) kurtosis (λ_4) on the rectangular step.

Appendix B. Separation of superharmonics

To analyze the temporal evolution of subharmonics and superharmonics at various positions, the signals must be decomposed. Initially, simple frequency-domain filtering (utilizing FFT and IFFT) can be applied to isolate frequency bands (Lin et al., 2019; Slunyaev, 2023; Slunyaev and Kokorina, 2023). However, for focused wave groups with wide frequency ranges, the spectral bands of higher-order harmonics inevitably overlap (e.g., the second superharmonics heavily overlap with the fundamental components). To overcome this and accurately extract overlapping components up to the fourth order, we employ the phase-manipulation approach established by Fitzgerald et al. (2014).

This method requires generating four identical wave groups with specific initial phase increments: $0°, 90°, 180°$, and $270°$. By linearly combining the corresponding recorded surface elevations (and their Hilbert transforms), the overlapping nonlinear components can be mathematically decoupled based on their order of phase dependence. The subharmonic frequency component and the fourth harmonic frequency component, which share the same phase dependency in this scheme, are subsequently separated via distinct frequency range filtering. The explicit mathematical formulations for these combinations are detailed in Fitzgerald et al. (2014) and are utilized here to systematically yield the decomposed harmonics η_1, η_2, η_3, and η_4.

Appendix C. Separation of second-order bound and free waves

In addition to separating superharmonics, the decomposition of wave profiles into free and bound wave components is also a problem to solve. The superharmonics normally represent the higher bound waves with the same velocity as the fundamental components. Water depth variation leads to higher-order bound and free waves. For the former, the frequency of the nth harmonic component is the n times peak frequency $f_{n,b} = nf_p$. The bound waves have the same phase speed as that of fundamental harmonics $c_{n,b} = c_1$, and the wavenumber $k_{n,b}$ equals n times nk_1. Newly free waves are generated in the spatial domain by meeting the relation $(n\omega_1)^2 = gk_{n,f}\tanh(k_{n,f}h_s)$ with h_s being the water depth in the shallower region. As a result, the phase speed of higher free waves is slower than that of bound waves $c_{n,f} < c_{n,b}$, which have the same frequencies $f_{n,f} = f_{n,b}$. For instance, the depth change induces components with the same frequency as bound waves but different velocities ($f_{2,b} = f_{2,f} = 2f_1, c_{2,b} \neq c_{2,f}$). The dispersion relations $D(\omega)$ calculating the wavenumber of second-order bound $k_{2,b}$ and free waves $k_{2,f}$ in the shallower regions h_s are $2D(\omega)$ and $D(2\omega)$, respectively,

$$k_{2,b} = 2k_1, \tag{14}$$

$$(2\omega)^2 = gk_{2,f} \tanh k_{2,f} h_s, \tag{15}$$

due to the same frequency of the free and bound waves, the higher free and bound waves cannot be separated from the frequency domain with the FFT or phase-manipulation method.

Through the phase-manipulation approach, the amplitudes of superharmonics can be obtained. It should be noted that because the phase-manipulation method separates components based on their order of nonlinearity, the extracted "nth harmonic" physically represents the entire nth-order harmonic band, intrinsically encompassing not only exact multiple harmonics ($n\omega_p$) but also all associated combinational frequencies (e.g., $\omega_i \pm \omega_j$). To further extract the wave profiles of second-order bound and free waves, the continuous wavelet transform (CWT) is introduced to process the data in both temporal and frequency domains. The different times of generation and velocities of free and bound waves make it possible to separate them from the spatio-temporal information with the CWT (Li and Ting, 2012).

In the time domain, the wavelet coefficients can be obtained by comparing the window signals at different positions one by one by moving the wavelet in time. A larger wavelet coefficient indicates a better match between the wavelet and the segment of the signal. In this process, the wavelet coefficient is obtained by convolving the wavelet with the signal over a window whose length is identical to that of the wavelet. Moreover, stretching or compressing the wavelet in the frequency domain adjusts both its length and frequency, making it possible to extract wavelet coefficients corresponding to different frequencies. Accordingly, the window length also varies with the wavelet length. Since the wavelets are compressed at high frequencies, the time window becomes narrower, resulting in a higher temporal resolution. The spatio-temporal wavelet coefficient map is obtained by combining the wavelet coefficients at different frequencies. With the decomposed second harmonics above, the spatio-temporal data of second superharmonics is obtained with the CWT. Then the separated second-order bound and free harmonics in the time domain can be inverted to the surface elevations. The CWT and inverse continuous wavelet transform (ICWT) adopt the adaptive solver available in many common software packages (Harang et al., 2012).

Data availability

Data will be made available on request.

References

Beji, S., Battjes, J.A., 1993. Experimental investigation of wave propagation over a bar. Coast. Eng. 19 (1–2), 151–162.

Benoit, M., Zhang, J., Ma, Y., 2024. Kinematics of nonlinear waves over variable bathymetry. Part I: Numerical modelling, verification and validation. Coast. Eng. 193, 104577.

Bolles, C.T., Speer, K., Moore, M., 2019. Anomalous wave statistics induced by abrupt depth change. Phys. Rev. Fluids 4 (1), 011801.

Choi, W., Camassa, R., 1999. Exact evolution equations for surface waves. J. Eng. Mech. 125 (7), 756–760.

Draycott, S., Li, Y., 2025. Extreme wave amplification through the interplay of wave nonlinearity and a two-dimensional bathymetry. Phys. Fluids 37 (2), 026617.

Draycott, S., Li, Y., Stansby, P., Adcock, T., Van den Bremer, T.S., 2022. Harmonic-induced wave breaking due to abrupt depth transitions: An experimental and numerical study. Coast. Eng. 171, 104041.

Ducrozet, G., Slunyaev, A., Stepanyants, Y., 2021. Transformation of envelope solitons on a bottom step. Phys. Fluids 33 (6), 066606.

Fitzgerald, C.J., Taylor, P.H., Taylor, R.E., Grice, J., Zang, J., 2014. Phase manipulation and the harmonic components of ringing forces on a surface-piercing column. Proc. R. Soc. A: Math. Phys. Eng. Sci. 470 (2168), 20130847.

Gramstad, O., Zeng, H., Trulsen, K., Pedersen, G., 2013. Freak waves in weakly nonlinear unidirectional wave trains over a sloping bottom in shallow water. Phys. Fluids 25 (12), 122103.

Harang, R., Bonnet, G., Petzold, L.R., 2012. WAVOS: a MATLAB toolkit for wavelet analysis and visualization of oscillatory systems. BMC Res. Notes 5 (1), 163.

Janssen, T., Battjes, J.A., Van Dongeren, A., 2003. Long waves induced by short-wave groups over a sloping bottom. J. Geophys. Res.: Ocean. 108 (C8), 8.

Kirby, J.T., Dalrymple, R.A., 1983. Propagation of obliquely incident water waves over a trench. J. Fluid Mech. 133, 47–63.

Kurkin, A., Semin, S., Stepanyants, Y.A., 2015. Transformation of surface waves over a bottom step. Izv. Atmos. Ocean. Phys. 51 (2), 214–223.

Li, Y., Chabchoub, A., 2023. On the formation of coastal rogue waves in water of variable depth. Camb. Prism.: Coast. Futur. 1, e33.

Li, Y., Draycott, S., Adcock, T.A., Van den Bremer, T.S., 2021a. Surface wavepackets subject to an abrupt depth change. Part 2. Experimental analysis. J. Fluid Mech. 915, A72.

Li, Y., Draycott, S., Zheng, Y., Lin, Z., Adcock, T.A., Van den Bremer, T.S., 2021b. Why rogue waves occur atop abrupt depth transitions. J. Fluid Mech. 919, R5.

Li, Z., Tang, T., Li, Y., Draycott, S., Van den Bremer, T.S., Adcock, T.A., 2023. Wave loads on ocean infrastructure increase as a result of waves passing over abrupt depth transitions. J. Ocean. Eng. Mar. Energy 9 (2), 309–317.

Li, F.-C., Ting, C.-L., 2012. Separation of free and bound harmonics in waves. Coast. Eng. 67, 29–40.

Lin, C.-K., Hsu, S.-Y., Lin, J.-G., 2019. FFT phase shift of water wave analysis. J. Mar. Sci. Technol. 27 (6), 4.

Liu, J., Xu, S., Mao, H., Han, C., Han, J., 2026. Modeling wave–structure interactions using fully nonlinear potential flow approach for deformable monopile foundations. Ocean Eng. 343, 123494.

Massel, S., 1983. Harmonic generation by waves propagating over a submerged step. Coast. Eng. 7 (4), 357–380.

Mei, C.C., 1989. The Applied Dynamics of Ocean Surface Waves. Advanced Series on Ocean Engineering. World Scientific.

Mondal, R., Alam, M.M., 2018. Water wave scattering by an array of rectangular breakwaters on a step bottom topography. Ocean Eng. 169, 359–369.

Monsalve, E., Maurel, A., Pagneux, V., Petitjeans, P., 2015. Propagation of nonlinear waves passing over submerged step. Phys. Procedia 70, 863–866.

Monsalve, E., Maurel, A., Pagneux, V., Petitjeans, P., 2022. Nonlinear waves passing over rectangular obstacles: multimodal method and experimental validation. Fluids 7 (5), 145.

Moore, N.J., Bolles, C.T., Majda, A.J., Qi, D., 2020. Anomalous waves triggered by abrupt depth changes: Laboratory experiments and truncated KdV statistical mechanics. J. Nonlinear Sci. 30, 3235–3263.

Moss, C.S., Schultz, D.M., Parkes, B., Li, Y., Draycott, S., 2025. Higher-harmonic contributions to surface elevation, kinematics, and wave loads in wave packets across an abrupt depth transition. Coast. Eng. 197, 104693.

Negi, P., Sahoo, T., Sriram, V., Stepanyants, Y., 2025. Wave scattering by an array of submerged bars: An analytic approach. Wave Motion 140, 103645.

Rapp, R.J., Melville, W.K., 1990. Laboratory measurements of deep-water breaking waves. Philos. Trans. R. Soc. Lond. Ser. A Math. Phys. Sci. 331 (1622), 735–800.

Salis, N., Hu, X., Luo, M., Reali, A., Manenti, S., 2024. 3D SPH analysis of focused waves interacting with a floating structure. Appl. Ocean Res. 144, 103885.

Samseth, K., Trulsen, K., 2025. Extreme statistics of wave forces on a horizontal cylinder behind a shoal. J. Fluid Mech. 1007, A59.

Schäffer, H.A., 1996. Second-order wavemaker theory for irregular waves. Ocean Eng. 23 (1), 47–88.

Slunyaev, A., 2023. Contributions of nonlinear spectral components to the probability distribution of rogue waves based on the results of numerical simulation of the Euler equations. Izv. Atmos. Ocean. Phys. 59 (6), 701–721.

Slunyaev, A.V., Kokorina, A.V., 2023. On the probability of down-crossing and up-crossing rogue waves. Phys. Fluids 35 (11), 117109.

Tang, T., Moss, C., Draycott, S., Bingham, H.B., Van den Bremer, T.S., Li, Y., Adcock, T.A., 2023. The influence of directional spreading on rogue waves triggered by abrupt depth transitions. J. Fluid Mech. 972, R2.

Trulsen, K., Raustøl, A., Jorde, S., Rye, L.B., 2020. Extreme wave statistics of long-crested irregular waves over a shoal. J. Fluid Mech. 882, R2.

Trulsen, K., Zeng, H., Gramstad, O., 2012. Laboratory evidence of freak waves provoked by non-uniform bathymetry. Phys. Fluids 24 (9), 097101.

Viotti, C., Dias, F., 2014. Extreme waves induced by strong depth transitions: Fully nonlinear results. Phys. Fluids 26 (5), 051705.

Viotti, C., Dutykh, D., Dias, F., 2014. The conformal-mapping method for surface gravity waves in the presence of variable bathymetry and mean current. Procedia IUTAM 11, 110–118.

Wu, Q., Feng, X., Dong, Y., Dias, F., 2023. On the behavior of higher harmonics in the evolution of nonlinear water waves in the presence of abrupt depth transitions. Phys. Fluids 35 (12), 127102.

Zhang, J., Benoit, M., 2021. Wave–bottom interaction and extreme wave statistics due to shoaling and de-shoaling of irregular long-crested wave trains over steep seabed changes. J. Fluid Mech. 912, A28.

Zhang, J., Ma, Y., Tan, T., Dong, G., Benoit, M., 2023. Enhanced extreme wave statistics of irregular waves due to accelerating following current over a submerged bar. J. Fluid Mech. 954, A50.

Zheng, Y., Lin, Z., Li, Y., Adcock, T., Li, Y., Van den Bremer, T.S., 2020. Fully nonlinear simulations of unidirectional extreme waves provoked by strong depth transitions: the effect of slope. Phys. Rev. Fluids 5 (6), 064804.